Journal Article

Machine learning-assisted direction-of-arrival accuracy enhancement technique using oversized lens-loaded cavity

Abbasi, M.A.B., Yurduseven, O., Akinsolu, M.O., Fusco, V.F., Liu, B., Khalily, M., Cotton, S.L. and Imran, M.A

Recommended citation:

IET Microwaves, Antennas & Propagation

The Institution of Engineering and Technology WILEY

ORIGINAL RESEARCH

Machine learning-assisted direction-of-arrival accuracy enhancement technique using oversized lens-loaded cavity

Muhammad Ali Babar Abbasi[1] | Okan Yurduseven[1] | Mobayode O. Akinsolu[2] |
Vincent F. Fusco[1] | Bo Liu[3] | Mohsen Khalily[4] | Simon L. Cotton[1] |
Muhammad Ali Imran[3]

[1]Institute of Electronics, Communications and Information Technology (ECIT), Queen's University Belfast, Belfast, UK

[2]Faculty of Arts, Science and Technology, Wrexham Glyndŵr University, Wrexham, UK

[3]James Watt School of Engineering, University of Glasgow, Glasgow, UK

[4]5GIC 6GIC, Institute for Communication Systems (ICS), University of Surrey, Guildford, UK

Correspondence

Muhammad Ali Babar Abbasi, Institute of Electronics, Communications and Information Technology (ECIT), Queen's University Belfast, Office 01/23, Northern Ireland Science Park, Queens Road, Queen's Island, Belfast BT3 9DT, UK.
Email: m.abbasi@qub.ac.uk

Funding information

Engineering and Physical Sciences Research Council, Grant/Award Numbers: EP/P000673/1, EP/S007954/1; Leverhulme Trust, Grant/Award Number: RL-2019-019

Abstract

This paper presents a framework for achieving machine learning (ML)-assisted direction-of-arrival (DoA) accuracy enhancement using a millimetre-wave (mmWave) dynamic aperture. The technique used for the enhanced DoA estimation accuracy leverages an over-sized lens-loaded cavity antenna connected to a single RF chain in the physical layer and a computational method in the computational layer of the framework. It is shown for the first time that by introducing a reconfigurable mode-mixing mechanism inside the over-sized lens-loaded cavity hardware, a greater number of spatially orthogonal radiation modes can be achieved giving rise to many cavity states. If the best cavity state is determined and selected by means of design exploration using a contemporary ML-assisted antenna optimisation method, the computational DoA estimation accuracy can be improved. The mode-mixing mechanism in this work is a randomly oriented metallic scatterer located inside an over-sized constant$-\epsilon_r$ lens-loaded cavity, connected to a stepper motor that is electronically controlled by inputs from the computational layer of the presented framework. Measurement results in terms of near-field radiation mode scans are included in this study to verify and validate that the proposed ML-assisted framework enhances the DoA estimation accuracy. Moreover, this investigation simultaneously provides a simplification in the physical layer implementation of mmWave radio hardware, and DoA accuracy enhancement, which in turn lends itself favourably to the adoption of the proposed framework for channel sounding in mmWave communication systems.

KEYWORDS

antennas, B5G mobile communication, channel estimation, diversity reception, lens antennas

1 | INTRODUCTION

Accurate, reliable, and fast, direction-of-arrival (DoA) estimation is vital for multi-user millimetre-wave (mmW) communication systems to function properly. This is especially true for communication channels with high mobility and shorter coherence time, where constant high-resolution channel sounding is required. Standard channel sounding techniques require an array of antennas connected to baseband processing units, where DoA estimation algorithms such as MVDR, MUSIC, ESPRIT and FT etc., are used [1–3]. Array-based

DoA estimation techniques are well known and are widely used in classical wireless communication systems, notably in sub-6 GHz 5G bands in recent times [4]. In mmWave communication systems (including mmWave 5G), using fully connected antenna arrays to enable mmWave DoA would require multi-fold hardware complexity; primarily due to, the path loss due must be compensated by increasing the number of antenna elements in the antenna arrays to achieve better array gains. In the context of channel sounder, this increases the number of RF chains [4, 5] and raises the hardware cost of mmWave channel sounding, making it unaffordable or

prohibitive for many cases. On other hand, using low-complexity hardware can compromise the angular discrimination of the DoA estimation. In addition, it negates the need for multiple RF chains, which require a higher degree of thermal considerations within the channel sounding hardware [6, 7].

The idea of using a single RF-chain architecture for DoA estimation is still in its infancy [8]. The practical implementation of this approach has been made possible by advances in the field of computational microwave imaging [9–13]. The concept has been verified in the literature via the reconstruction of the scene information and then compressing and passing it over via a single RF chain using a frequency-diverse antenna, which faces the scene [10–14].

In this work, a structural modification of previously studied DoA estimation approaches in Ref. [15, 16] is presented using an ML-based framework. Using this framework, it is shown for the first time that the accuracy of computational DoA estimation can be improved by converting simple lens-loaded cavity hardware into a lens-loaded dynamic aperture that can be optimised using a contemporary ML-assisted optimisation technique. To achieve this enhancement in DoA estimation accuracy, the only modification required in the physical layer of the proposed framework is the addition of a mechanically controlled mode-mixing scatterer placed inside the cavity. The ML-assisted optimisation and DoA estimation, both occur in the computational layer of the framework.

By studying the lens-loaded cavity radiation modes carefully and optimising them with respect to the given channel condition (feedback through the computational layer), enhanced accuracy in DoA estimation is feasible. The system-level operations of the presented framework are shown in the block diagram in Figure 1. The benefit of placing a constant $-\epsilon_r$ lens in front of the cavity is thoroughly discussed in a previous investigation, Ref. [15], while this work focusses on the framework that demonstrates how a single-state lens-loaded cavity can be converted into a multi-state cavity and how an ML-assisted optimisation of this multi-state cavity can positively impact the spatial-temporal bases for enhanced accuracy of DoA estimation.

The ML-assisted optimisation technique used in the proposed framework (Figure 1) is the first-generation method in the surrogate model-assisted differential evolution for antenna synthesis (SADEA) series of algorithms [17–21]. SADEA-I is adopted in this work as it has been shown to provide up to 20 times speed improvement in comparison to standard global optimisation methods for antenna optimisation, while also converging to better design solutions [22, 23]. The efficiency improvement in SADEA-I comes from a harmonious balance between evolutionary search (i.e. revised differential evolution (DE) operators) to explore the antenna's design space, and the Gaussian Process (GP) ML-based surrogate models for predicting antenna's performances [17]. The optimal co-use of evolutionary search and surrogate modelling in the kernel of the optimisation is achieved by the surrogate model-aware evolutionary search (SMAS) framework [22] for surrogate model management.

The contribution of this work is twofold. First, we propose a novel lens-loaded dynamic aperture structure that has the capability to update its radiation mode states by as little as 1° of mechanical rotation of a mode-mixing scatterer. Second, we propose a framework to optimise the lens-loaded cavity states using SADEA-I to achieve an enhanced DoA estimation accuracy.

2 | LENS-LOADED DYNAMIC APERTURE HARDWARE

The physical layer of the framework in Figure 1 comprises a dynamic aperture constructed using a frequency-diverse chaotic cavity, a constant$-\epsilon_r$ lens, a mode-mixing mechanism, and a stepper motor. This lens-loaded dynamic aperture is connected to the computational layer of the framework via an RF chain (not shown in Figure 1 for brevity). The structural configuration of the dynamic lens-loaded aperture is shown in Figure 2a, where a metallic box is constructed to form a chaotic cavity, a constant$-\epsilon_r$ lens is placed on one side of this metallic box (facing the $+z-$ axis), while the RF-chain input/output is on the opposite side of the lens (facing the $-z-$ axis). Note that the chaotic cavity and the lens structure are the same and used previously in Ref. [15, 16]. A purposely created surface with sub-wavelength holes is connected to the chaotic cavity, acting as a medium of electromagnetic (EM) energy coupling between the chaotic cavity and the lens surface. The physical dimensions of the lens structure, the cavity, and the location of the RF-chain input/output are shown in Figure 2a. Further details around the construction of the chaotic cavity, the constant$-\epsilon_r$ lens, and the rationale behind the selection of the hardware and structural specifications can be found in Ref. [15].

The most important component of the physical layer in the proposed framework, relevant to the investigation presented here is the mode-mixing mechanism from Figure 1. The mode-mixing mechanism is controlled by a stepper motor that receives feedback dynamically, from the computational layer of the proposed framework. The mode-mixing mechanism comprises a mode-mixing scatterer (a metallic plate) hanging from the top, inside the cavity as shown in Figure 2a and b. This randomly oriented metallic scatterer is responsible for reflecting and mixing EM fields within the cavity. A few considerations are important for the mode-mixing scatterer. First, it is important that the scatterer is not placed exactly at the centre of the cavity since it is desirable to break the structural symmetry inside the chaotic cavity along all three axes [24].
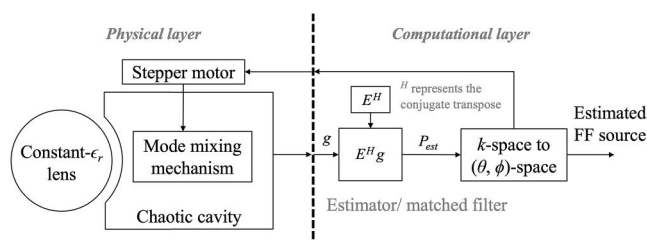

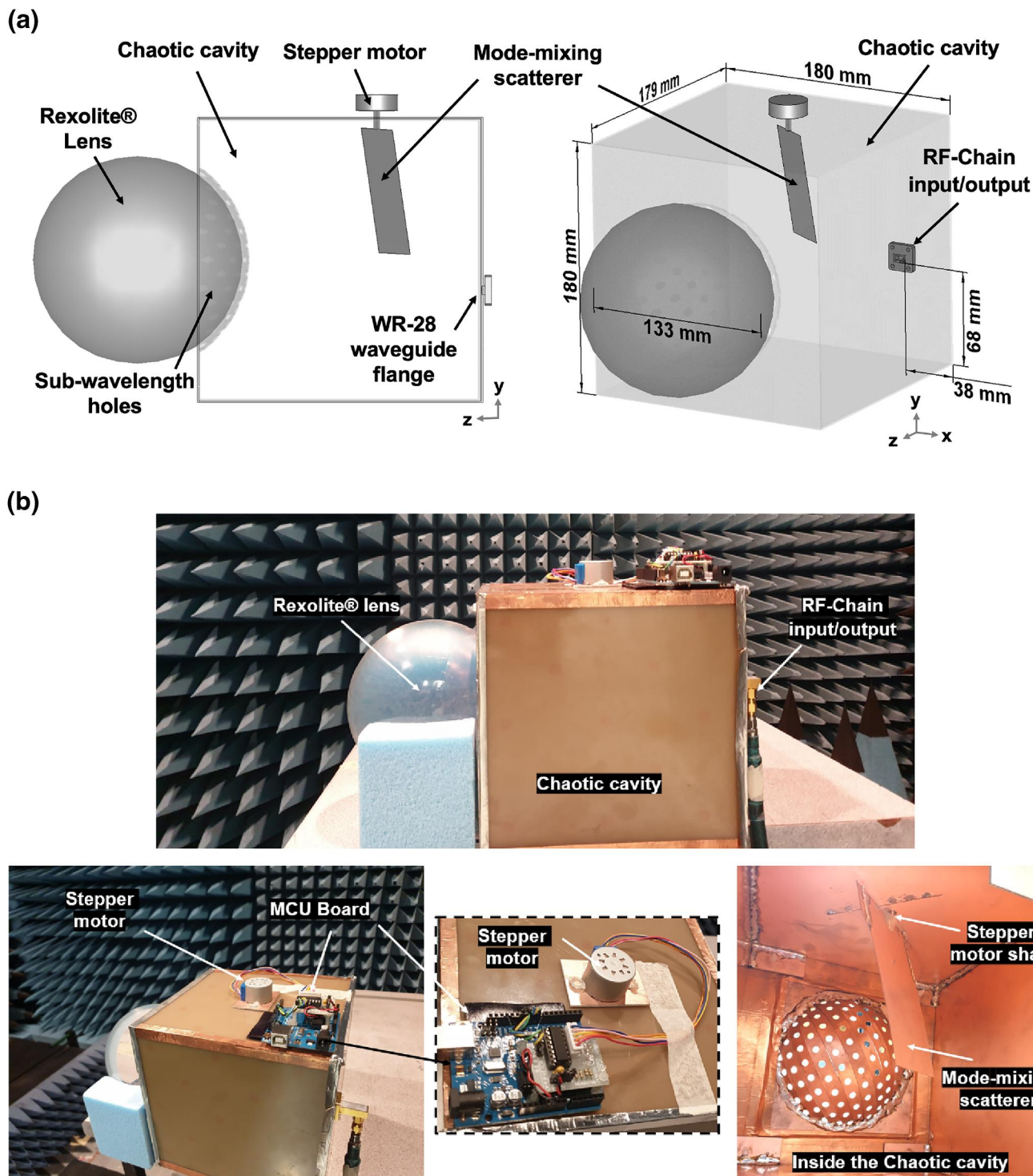**FIGURE 1** System level block diagram

(a)

(b)

FIGURE 2 Frequency-diverse over-sized chaotic cavity with constant−ϵ_r lens having a mechanically rotatable mode-mixing scatterer operating as a dynamic lens-loaded aperture as a (a) geometrical configuration of the dynamic lens-loaded aperture. (b) Fabricated prototype placed in an anarchic chamber to verify dynamic aperture operation via near-field measurements

Second, the mode-mixing scatterer must not touch any of the chaotic cavity wall, and this should be the case for all rotations of the stepper motor (0° − 360°). Lastly, the mode-mixing scatterer needs to be firmly fixed from the stepper motor shaft such that its location at any given angular rotation of the stepper motor is fixed.

Figure 2b shows the hardware of the dynamic lens-loaded cavity. The metallic cavity structure is built using single-sided metallised substrate sheets. The curved surface with sub-wavelength holes is developed separately and soldered inside the cavity such that a portion of the cavity structure hosts the spherical constant−ϵ_r lens [15, 25]. The lens was developed

using Rexolite material with the relative permittivity (ϵ_r) of 2.53 and loss tangent ($\tan(\delta)$) of 0.00066. The spherical radius of the sub-wavelength hole is determined according to the principle of Petzval curvature [26] that enables a gap between the sub-wavelength hole surface and the lens surface. Note that for a constant−ϵ_r lens of this kind, the focal point of the impinging plane wave lies outside of the lens surface. The sub-wavelength hole surface is exactly at the focal length. The structure is developed to operate at a central frequency of 28 GHz over a bandwidth from 27 to 29 GHz. At the rare side of the cavity, an RF chain with the same bandwidth is connected via WR28 waveguide to the K-type converter for EM signal input/output. The mode-mixing scatterer is rigidly connected to the stepper motor shaft inserted within the cavity from the top. The stepper motor is placed outside the cavity and is connected to an Arduino UNO board responsible for generating rotation angle commands using a microcontroller (Microchip Atmel ATmega328P).

3 | DYNAMIC APERTURE OPERATION FRAMEWORK

It has been shown previously that the DoA of an impinging EM wave can be computed using a set of compressive measurements in a frequency-diverse structure [8]. This concept has also been applied to a radiating cavity-backed wall with sub-wavelength holes, as documented in the literature on computational imaging [10]. When an EM signal is excited from the input of a frequency-diverse cavity, it radiates spatially orthogonal field radiation modes towards the field-of-view (FoV) and the quasi-randomness of these modes is helpful in encoding the impinging plane wave information. The main purpose of a mode-mixing scatterer is to enhance this quasi-randomness of the cavity by dynamically updating the reflections of the EM energy trapped inside the chaotic cavity. Note that the mode-mixing method in this work is similar to the methods described in Ref. [9, 11] and the references therein. However, it is dynamic and unique because the field radiation modes are observed by means of a simple rotation of a mode-mixing scatterer (Figure 2b) controlled by a stepper motor for generating a new set of quasi-random radiation fields.

As a demonstration of the capability of the hardware described above, let us consider the E-field measured and plotted at an observation plane which is 0.4 m away from the cavity aperture (distance along z-axis between the spherical lens edge and the observation plane) at a single frequency (28 GHz) when the only change that happens within the cavity is the rotation of mode-mixing scatterer from 1° to 2° and then to 3°. A unique set of magnitude and phase masks are observed for all three rotation conditions.(see Figure 3) This feature is exploited to convert a chaotic cavity into a dynamically reconfigurable chaotic cavity to achieve a much greater number of field radiation modes than it is physically possible when only a single static state of lens-loaded cavity is considered. To determine the best lens-loaded cavity state, hence, the

most suitable mode-mixing scatterer angle of rotation, a computational space is created by formulating a 1-D optimisation problem to find the best state of the lens-loaded cavity for a given channel. Although not verified in this study, it can be argued that if the 1-D optimisation problem is computationally fast enough, finding the best state of the lens-loaded cavity for a given channel, and the subsequent physical implementation can be carried out in real-time. Here, fast enough means the computational time is at least faster than one coherence time cycle of the mmWave channel.

Based on the above discussion, the framework proposed for the dynamic lens-loaded cavity optimisation considers the wave-chaotic transfer function. Considering that the field projected by a single state of the lens-loaded cavity on a measurement plane is $E(r, w, k)$, the impinging signal from multiple sources on the lens-loaded cavity is defined by P, and the compressed measurements are g, then the relationship between them can be written as follows [8, 15]:

$$g(w) = \int_r E(r, w, k)P(r)dr + n \qquad (1)$$

where, n is the system noise, r defines the coordinates across the aperture, w is the frequency and k is the current lens-loaded aperture state. Using (1), an estimate of the signal, P_{est}, can be computed by means of matched-filtering, $P_{est} = E^\dagger g$, as shown in the computational layer of Figure 1. Hence, a Fourier transform operation on P_{est} can produce the DoA estimation pattern, from which the DoA information can be retrieved using a peak-finding algorithm. Moreover, the DoA estimation can be evaluated using the iterative method for one state of the lens-loaded cavity [8].

Now, let us consider that the static (first state) of the lens-loaded cavity is updated using the mode-mixing mechanism, and the set of modes generated by the previous state, $E(r, w, k)$, are no longer valid. At this stage, the cavity is moved to a new state with a new set of modes. In the computational layer of the proposed framework, previously estimated P ($P_{est,M,1}$) and their $E(r, w, k)$ can be buffered for comparisons with the new lens-loaded cavity states ($P_{est,M,2}$) and their $E(r, w, k)$ using SADEA-I. More explicitly, if P_{state} is the database for the lens-loaded cavity state designs in the SADEA-I-based aperture optimisation process and x in [0°, 360°] is any single lens-loaded cavity state design within P_{state}, P_{state} is initialised with a population of α lens-loaded cavity state designs (generated by Latin Hypercube sampling method [27]) and their measured field radiation modes on the reference plane.

After initialisation, in each iteration of SADEA-I, child solutions are generated by applying DE mutation and crossover operations to a fixed number (λ) of top-ranked lens-loaded cavity state designs selected from P_{state}. GP is then used to construct surrogate models for each lens-loaded cavity state design in each child population using the nearest designs (based on Euclidean distance) from P_{state} and their measured field radiation modes on the reference plane as training data points.

The generated child solutions are prescreened using the lower confidence bound method [28] to handle prediction
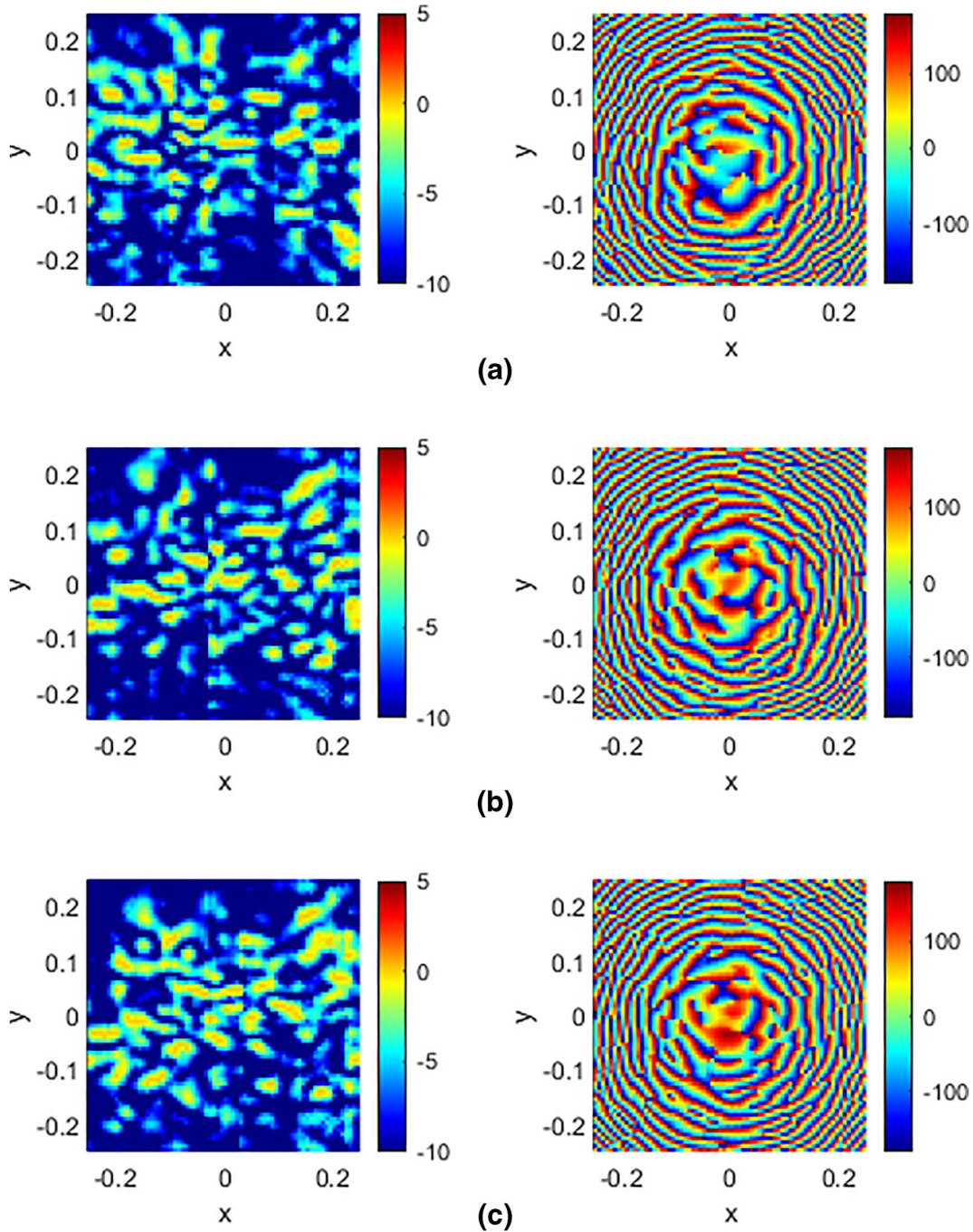
FIGURE 3 Experimental *E*-field magnitude and phase recorded on a near-field reference plane at a single radiation mode (i.e. 28 GHz) for three different dynamic lens-loaded cavity states. Colour bar is in dB scale (left column) and degree scale (right column). *x* and *y* are in metres. (a) State at 1° rotation. (b) State at 2° rotation. (c) State at 3° rotation

uncertainty. The lower confidence bound values are then ranked, and the best of them is simulated. The process is repeated until a stopping criterion such as the maximum number of objective function evaluations (N_{eval}) is met. For our investigations, we have typified the ML-assisted optimisation process using the measured data discussed in Section 4, and the following settings have been used for SADEA-I: $\alpha = 20$, $\lambda = 20$, and $N_{eval} = 150$. All other algorithmic parameters for SADEA-I are used according to Ref. [17].

4 | MEASUREMENTS, RESULTS AND DISCUSSION

To evaluate the performance of the proposed ML-assisted DoA accuracy enhancement framework presented in the previous section, the lens-loaded dynamic aperture was placed in a near-field anechoic chamber and connected to a signal generator. Considering the first static state, the lens-loaded cavity was excited by 41 single frequency signals from 27 to 29 GHz.

The complex *E*-field was measured in an observation plane of length (along *x*-axis) and width (along *y*-axis) equals to 0.5 m for all frequency samples. The total number of observation points against each of the 41 frequency inputs was 71 × 71, making a single lens-loaded cavity state near-field measurements of 5041 × 41 for each cavity state for the entire bandwidth. To avoid an extremely large dataset, the rotation of the stepper motor was confined to the range 0° − 90° with a step size of 1°, creating an overall measurement dataset size of about 40 Gigabytes. The memory corresponding to one angular measurement is ∼444 Megabytes per cavity state for the entire bandwidth. The ML process in this case is data driven, which means it uses the measured values, making it computationally inexpensive. Moreover, the matched-filter problem (see Figure 1) took 2.6 ms, averaged over 10 reconstructions on an Intel i7 CPU and 128 GB RAM machine.

4.1 | DoA estimation accuracy enhancement

To understand the extent of DoA estimation accuracy enhancement, the DoA estimation patterns are examined for three plane waves, originating from three different far-field sources and impinging on the lens-loaded cavity as shown in Figure 4. In Figure 5, a comparison is given between the DoA estimation patterns using a non-optimised state of the lens-loaded cavity (considered as the reference) and an optimised state of the lens-loaded cavity after passing through the ML-assisted DoA accuracy enhancement framework. From Figure 5, the improved fidelity of the DoA pattern retrieved using the optimised cavity is evident. Note that the DoA estimation patterns are computed in a post-processing stage to mimic the computational layer using the measurement dataset.

Considering a single state of the lens-loaded cavity of the size shown in Figure 1a, based on the *Q*-factor, a much larger number of measurement modes are theoretically possible. However, it is shown that the DoA estimation using a single state of the cavity is still possible using only 41 measurement modes within the 27–29 GHz bandwidth. This is realised by relaxing the computational problem and restricting the dimensions of the unknowns to only consider the transverse components of impinging plane wave vector. It is also important to note that the power spectrum of the source field

impinging upon the lens-loaded cavity is assumed to be constant over the entire bandwidth of interest. This assumption is valid since the fractional bandwidth under consideration is relatively small (i.e. only 7% in this case) [8]. This assumption is used only to simplify the mathematical model used for the far-field sources and is the same for both non-optimised and optimised cavity states.

A comparison between the ground truth DoA and the estimated incident angles is given in Tables 1 and 2 for the non-optimised and optimised cavity states. It can be seen that the DoA estimation has been possible for only two out of the three impinging signals (Source 2 and Source 3) using the non-optimised cavity state while the estimation accuracy is also low (see Figure 5a). On the other hand, under the same physical conditions, just by controlling the rotation of the stepper motor, estimation of all three sources has been possible after reaching the optimised lens-loaded cavity state. It can also be observed that the DoA estimation is more accurate in Table 2 in comparison to the DoA estimation in Table 1, verifying the operation of the proposed framework. It should be noted here that the selection of three far-field sources, as well as their incident angles, is arbitrary, and a similar analysis can be carried out using a different number of far-field sources and incident angles. It is worth mentioning that the DoA estimation accuracy of very closely spaced and overlapping sources is not addressed in this investigation.

4.2 | Noise analysis

The DoA estimation study carried out in the previous subsection does not take noise into account; hence, the signal-to-noise ratio (SNR) is considered infinite. To better replicate practical wireless channels, noise is introduced in the measurements such that the SNR level is brought down to practical levels. To do this, additive white Gaussian noise (AWGN) is introduced into the measurement dataset, while the DoA estimation accuracy enhancement of the lens-loaded cavity is tested at varying SNR levels ranging from 0 dB to 20 dB. In conformity to conventional signal processing routines, the probability density function of the introduced AWGN is equal to that of standard normal distribution and it is characterised by a bell-shaped curve with a mean value of null, standard
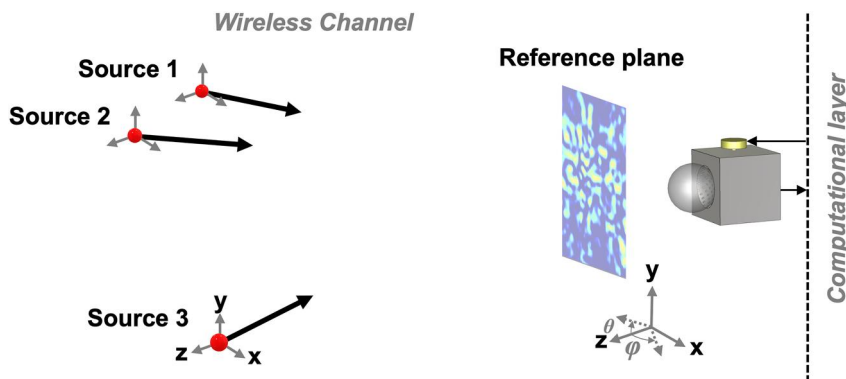

FIGURE 4 Illustration of the experimental setup to investigate the DoA estimation accuracy enhancement
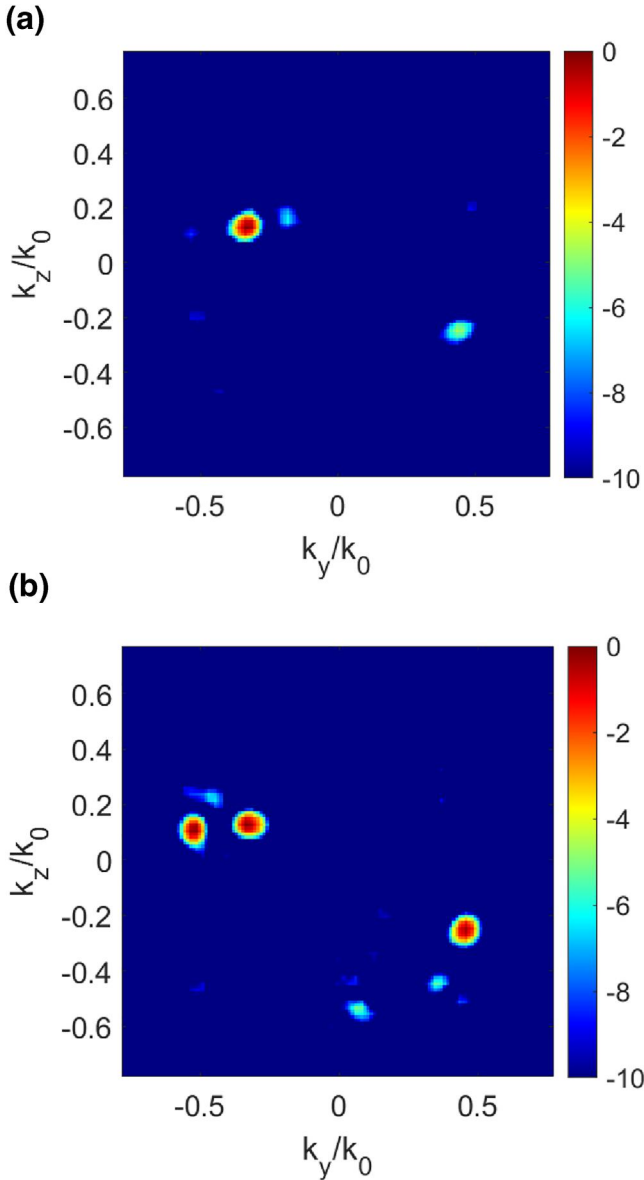
(a)

(b)

FIGURE 5 Reconstructed DoA estimation patterns (normalised; colour bar is in dB scale) for three sources, when dynamic lens-loaded cavity is: (a) Not optimised. (b) Optimised

TABLE 1 DoA using non-optimised lens-loaded dynamic aperture

	Incident angle (Ground truth)	Incident angle (Estimated)
Source 1	$\theta_1 = -30°, \phi_1 = -15°$	Not detected
Source 2	$\theta_2 = -20°, \phi_2 = -20°$	$\theta_{2,est} = -20.7°, \phi_{2,est} = -21°$
Source 3	$\theta_3 = 30°, \phi_3 = -25°$	$\theta_{3,est} = 30.1°, \phi_{3,est} = -29.5°$

TABLE 2 DoA using optimised lens-loaded dynamic aperture

	Incident angle (Ground truth)	Incident angle (Estimated)
Source 1	$\theta_1 = -30°, \phi_1 = -15°$	$\theta_{1,est} = -30.7°, \phi_{1,est} = -14.8°$
Source 2	$\theta_2 = -20°, \phi_2 = -20°$	$\theta_{2,est} = -20.8°, \phi_{2,est} = -20.7°$
Source 3	$\theta_3 = 30°, \phi_3 = -25°$	$\theta_{3,est} = 30.3°, \phi_{3,est} = -25.1°$

three far-field sources. On the other hand, the optimised lens-loaded cavity state can accurately retrieve the DoA of all three far-field sources at SNR levels of 5 dB, 10 and 20 dB. DoA estimation has only been impossible for one of the far-field sources at SNR = 0 dB, showing that even the optimised lens-loaded cavity state cannot compensate for the loss of signal due to high channel noise levels. Nevertheless, Figure 7 confirms that the proposed DoA estimation accuracy enhancement framework operates well in practical noise conditions.

4.3 | Effect of phase synchronisation

For the studies presented in Sections 4.1 and 4.2, it was assumed that the far-field sources share the same phase reference. In practical applications, far-field sources for DoA estimation do not necessarily need to be phase-synchronised. In other words, the phase coherence between the individual sources can be defined on an arbitrary basis, and the presented technique should be applicable to such scenarios to be considered useful for practical applications. To this end, we re-study the DoA estimation scenario, originally presented in Figure 5b, with the optimised cavity. In this new study, we consider two scenarios: (a) each far-field source is assigned to an individual, arbitrarily defined phase reference, and (b) the far-field sources share the same phase reference. For the phase-asynchronous case, the phase references of source 1, source 2 and source 3 are varied by $\pi/6$ radians, $\pi/4$ radians, and $\pi/3$ radians, respectively. It should be noted here that the selection of these reference phase variation values is done on an arbitrary basis, and a similar analysis can be carried out for different phase reference values without loss of generality. The retrieved DoA patterns are shown in Figure 8.

As can be seen in Figure 8, breaking the phase-synchronisation between the far-field sources does not alter the accuracy of the presented technique. This is because the technique is sensitive to the relative phase pattern of the
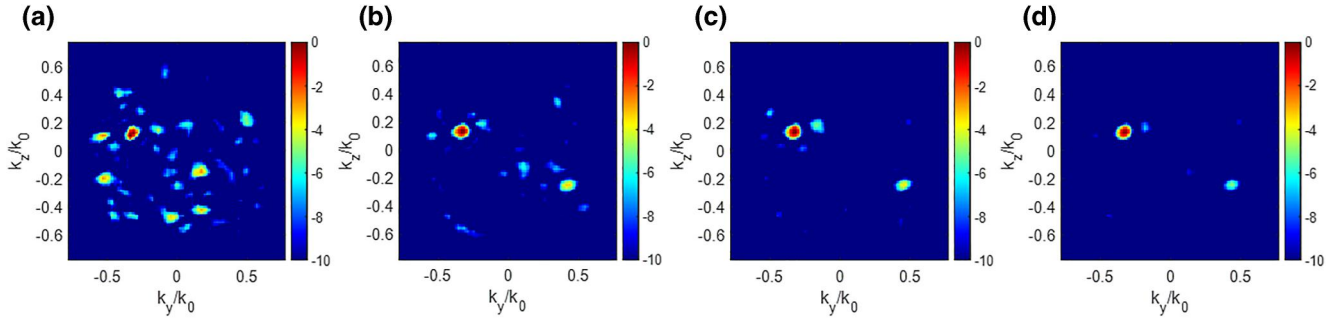
deviation of unity and total area (under the curve) of unity. Individual DoA estimations are then performed for the non-optimised and the optimised states of the lens-loaded cavity in the presence of three simultaneous far-field sources, having ground truth DoA same as the ones shown in Tables 1 and 2. The estimated DoA patterns are presented in Figure 6 and Figure 7 for non-optimised and optimised lens-loaded cavity states, respectively.

It can be observed that using a non-optimised cavity state, the retrieval of DoA estimation patterns for the impinging signals from a maximum of only two far-field sources is possible at high SNR levels (20 and 10 dB), while the DoA estimation is not clear for low SNR levels (5 and 0 dB). This also confirms that even at high SNR levels, the lost DoA information has not been successfully retrieved considering all

FIGURE 6 Retrieved DoA estimation patterns (normalised; colour bar is in dB scale) of three simultaneous sources using the initial state of the lens-loaded cavity at varying noise levels when: (a) SNR = 0 dB. (b) SNR = 5 dB. (c) SNR = 10 dB. (d) SNR = 20 dB
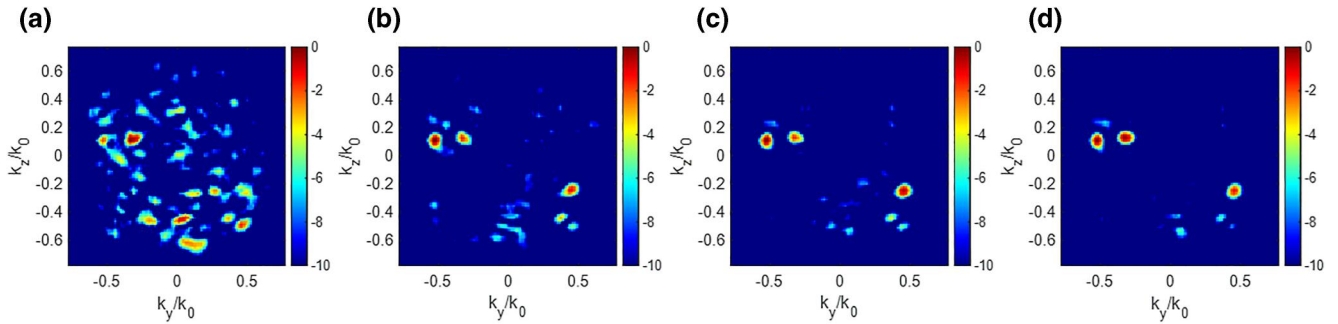

FIGURE 7 Retrieved DoA estimation patterns (normalised; colour bar is in dB scale) of three simultaneous sources using the optimised state of the lens-loaded cavity at varying noise levels when: (a) SNR = 0 dB. (b) SNR = 5 dB. (c) SNR = 10 dB. (d) SNR = 20 dB

impinging signals projected onto the cavity aperture, which is controlled by the incident angles, (θ, ϕ) [8, 15], rather than the absolute phase offsets that can be added to the projected field patterns.

4.4 | Impact of rotation resolution

In this subsection, the impact of the stepper motor's rotation resolution on the optimisation time and the DoA estimation accuracy is examined. The algorithm run-time is subjective, depending upon the computational power of the platform to be used at the computational layer of Figure 1. Similarly, the time required for the mode-mixing scatterer to get to a new state is also subject to the physical layer hardware specifications (cavity, stepper motor, microcontroller etc.). Therefore, a good way to infer the optimisation speed is to use the number of iterations required by the SADEA-I to converge to an optimised cavity state. Figure 9 presents a comparison between the number of iterations required when the lens-loaded cavity is separately optimised with a stepper motor rotation resolution of 1°, 2°, 4° and 8°, respectively. The minimum average correlation coefficient is used as the criterion to compare the performance of resulting cavity states, since it is inversely proportional to the DoA estimation accuracy (see Ref. [15] for proof). Each point along the x-axis in Figure 9 represents a distinct cavity

state, while the values on the y-axis represent the correlation coefficient and minimum correlation coefficient computed using all 41 measured field radiation modes for that particular cavity state.

When the optimisation framework is operational, the computational layer keeps updating the state of the cavity and the minimum correlation coefficient value is computed for every update. If the computed correlation coefficient for the current cavity state is better than the previously computed value, the algorithm supersedes the previous best; otherwise, it keeps the previous best value. The algorithm stops after reaching the maximum allowable number of iterations, defining the final minimum correlation coefficient value for the optimised cavity state. The results in Figure 9 typify the trade-off between the better cavity state (better DoA estimation) and the rotation resolution (faster optimisation). When the step size is 1° is used, the algorithm takes 20 + iterations, to provide an optimised cavity state. The number of iterations decreases to 8 + , meaning faster convergence of the optimisation framework, but at a cost of a higher correlation coefficient value. Intuitively, a larger angular resolution for varying the stepper motor means a reduced design search space and a somewhat low-cost implementation (in terms of computational overhead) and vice versa. However, sparse data (based on a larger step size or angular resolution) also means that the accuracy of the entire process is lowered.
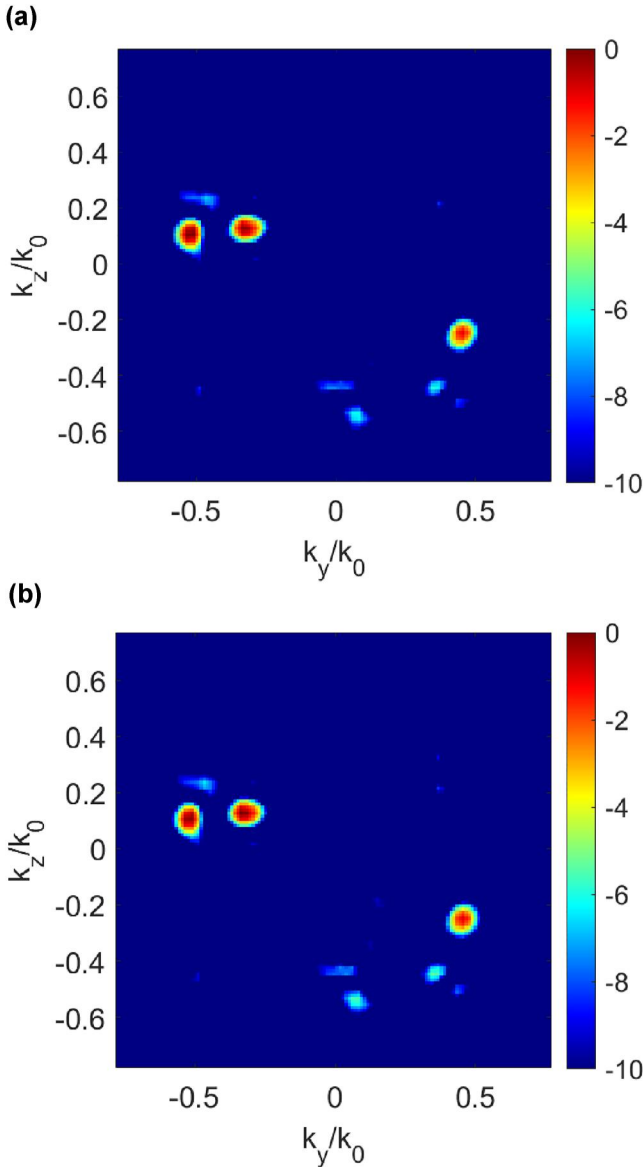
(a)

(b)

FIGURE 8 Reconstructed DoA estimation patterns (normalised; colour bar is in dB scale) for three sources, when dynamic lens-loaded cavity is: (a) Far-field sources have arbitrarily defined phase references (phase-asynchronous). (b) Far-field sources share the same phase reference (phase-synchronous)
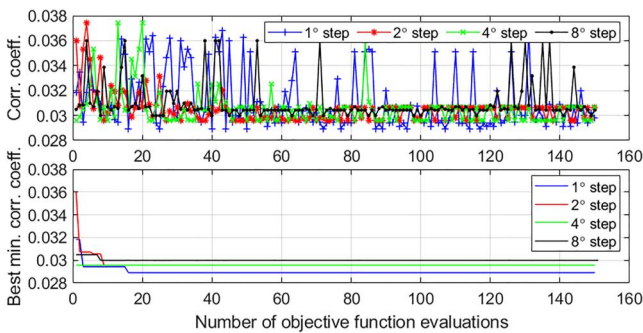

FIGURE 9 Trends for the SADEA-I optimisation

This expected degradation is not observed for angular resolutions of 2° and 4°.

Now let us compare the DoA estimation patterns computed using non-optimised cavity states, and cavity states separately optimised using 1°, 2°, and 8° of the stepper motor rotation resolution. The results are presented in Figure 10. The patterns reveal that the DoA estimation accuracy is better when 1° rotation resolution is used; however, the time to optimise is the highest (see Figure 9). It can also be seen that the DoA estimation using cavity states that are optimised using 2° rotation resolution is also accurate; however, the number of iterations required to get to this state is almost halved. These two results typify a very useful trade-off between the DoA estimation accuracy, and the time required to achieve an optimised solution, leading to a possibility of load balancing between the physical layer and the computational layer (Figure 1) by carefully selecting the rotation resolution.

4.5 | Singular value decomposition analysis

When applied to antenna-radiated field modes, the singular value decomposition (SVD) technique can constitute a measure of the diversity of the field patterns radiated by any single state of the lens-loaded cavity while facing the FoV [6, 8]. The optimisation framework presented in the previous section improves the orthogonality between the radiated field modes of neighbouring frequencies. This can be observed from the SVD contour shown in Figure 11 for a comparison between the non-optimised and the optimised lens-loaded cavity states at multiple rotation resolutions. For this analysis, considering σ_{max} to be the maximum singular value and σ_{min} to be the minimum singular value, the condition number for the non-optimised lens-loaded cavity state can be deduced as: $\sigma_{max}/\sigma_{min} = 35.83$, while for the optimised state (1° step size) it is: $\sigma_{max}/\sigma_{min} = 16.03$. In other words, the condition number of the optimised cavity is 55.2% smaller than the non-optimised cavity. Note that for an ideal case (i.e. best-case scenario), the condition number is unity (i.e. $\sigma_{max}/\sigma_{min} = 1$). Therefore, it can be said that the optimised cavity state using any rotation resolution, including 2° and 8° steps, is better when compared to the non-optimised cavity state, confirming the utility of the proposed ML-assisted DoA estimation enhancement framework.

5 | CONCLUSION

This paper presented an ML-assisted optimisation framework implemented on a dynamic lens-loaded aperture-based system for the purpose of DoA estimation. The presented hardware is unique in that it has the capability to improve itself based on the ML-assisted optimisation parameters. The system consists of a mode-mixing scatterer, strategically placed inside a lens-loaded wave chaotic cavity, which can be controlled by
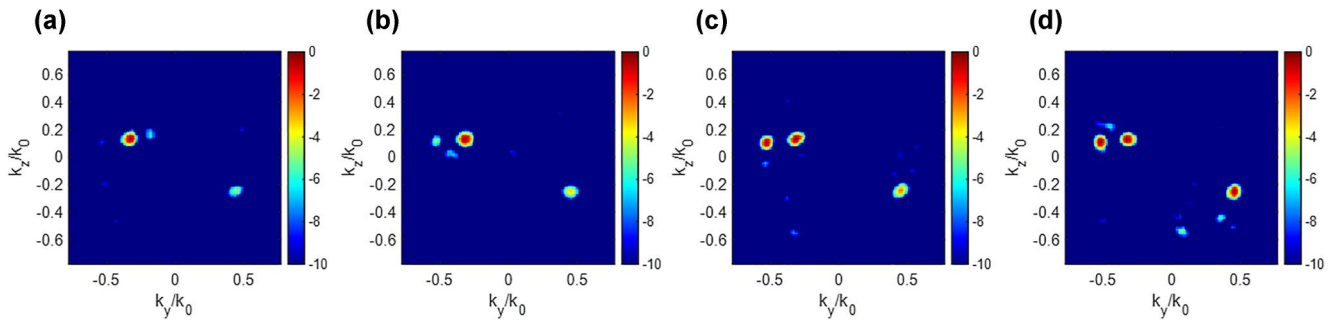
FIGURE 10 DoA estimation patterns using non-optimised and optimised lens-loaded cavity states with different stepper motor rotation resolutions. Colour bar is in dB scale. (a) Non-optimised, (b) Optimised; 8° rotation resolution, (c) Optimised; 2° rotation resolution and (d) Optimised; 1° rotation resolution
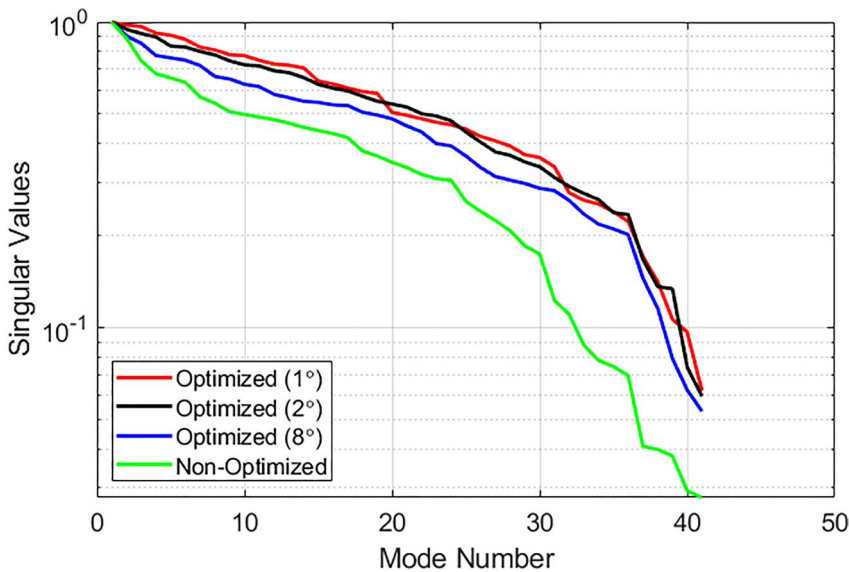

FIGURE 11 Comparison between measured singular values of the initial state and the optimised states of the dynamic lens-loaded cavity

a stepper motor to have any orientation between $0° - 360°$ with a step size ranging from as little as 1° to 8°. It was shown that the mode-mixing scatterer has the capability of updating the state of the lens-loaded cavity, turning it into a dynamic aperture just by updating its angle of rotation. The cavity structure, and its extension, the dynamic aperture is sensitive to any change within the cavity and creates a unique set of quasi-random radiation modes. The optimum state of the lens-loaded cavity can be selected by using SADEA-I, eventually leading to enhanced DoA estimation of multiple impinging signals. The framework was thoroughly tested and verified using extensive experimental datasets. DoA estimation accuracy enhancement was confirmed by studying DoA estimation patterns in the absence as well as in the presence of noise. Lastly, the mathematical conditioning improvement using the proposed ML-assisted framework was verified by comparing the singular values of multiple optimised and non-optimised cavity states. The future direction for this work will include investigating DoA estimation performance using non phase-synchronised signal sources and ML-assisted optimisation of the lens-loaded cavity based on the channel state information.

CONFLICT OF INTEREST STATEMENT

There is no conflict of interest.

DATA AVAILABILITY STATEMENT

The data that support the findings of this study are available from the corresponding author upon reasonable request.

ORCID

Muhammad Ali Babar Abbasi https://orcid.org/0000-0002-1283-4614
Okan Yurduseven https://orcid.org/0000-0002-0242-3029

REFERENCES

1. Gao, F., Gershman, A.B., Gershman, A.B.: A generalised ESPRIT approach to direction-of-arrival estimation. IEEE Signal Process. Lett. 12, 254–257 (2005)

2. Zhang, X., et al.: Reduced-complexity capon for direction of arrival estimation in a monostatic multiple-input multiple-output radar. IET Radar, Sonar Navig. 6, 796–801 (2012)

3. Mohanna, M., et al.: Optimisation of music algorithm for angle of arrival estimation in wireless communications. NRIAG J. Astron. Geophys. 2, 116–124 (2013)

4. Bas, C.U., et al.: Real-time millimetre-wave MIMO channel sounder for dynamic directional measurements. IEEE Trans. Veh. Technol. 68(9), 8775–8789 (2019)

5. Bjornson, E., et al.: Massive MIMO in sub-6 GHz and mmWave: physical, practical, and use-case differences. IEEE Wireless Commun. 26(2), 100–108 (2019)

6. Aslan, Y., et al.: Thermal-aware synthesis of 5G base station antenna arrays: an overview and a sparsity-based approach. IEEE Access. 6, 58868–58882 (2018)

7. Chiu, C.-P.: Heat sink for 5G massive antenna array and methods of assembling same. U.S. Patent No. 10. 320, 051 (2019)

8. Yurduseven, O., et al.: Frequency-diverse computational direction of arrival estimation technique. Sci. Rep. 9(1), 1–12 (2019)

9. Yurduseven, O., et al.: Computational microwave imaging using 3D printed conductive polymer frequency-diverse metasurface antennas. IET Microw., Antennas Propag. 11(14), 1962–1969 (2017)

10. Zhao, M., et al.: Frequency-diverse bunching metamaterial antenna for coincidence imaging. Materials. 12(11)1817 (2019)

11. Fromenteze, T., et al.: Computational imaging using a mode-mixing cavity at microwave frequencies. Appl. Phys. Lett. 106(19), 194104 (2015)

12. Yurduseven, O., et al.: Lens-loaded coded aperture with increased information capacity for computational microwave imaging. Rem. Sens. 12(9), 1531 (2020)

13. Hoang, T.V., et al.: Spatial diversity improvement in frequency-diverse computational imaging with a multi-port antenna. Results Phys. 22, 103906 (2021)

14. Fromenteze, T., et al.: Computational polarimetric microwave imaging. Optics expres. 25(22), 27488–27505 (2017)

15. Abbasi, M.A.B., et al.: Frequency-diverse multimode millimetre-wave constant-ϵ_r lens-loaded cavity. Sci. Rep. 10(1), 1–12 (2020)

16. Abbasi, M.A.B., Fusco, V.F., Yurduseven, O.: Millimetre-Wave channel sounding technique using oversized lens–loaded cavity. In: 2021 Proc. 15th European Conf. On Ant. Propag. (EuCAP). Düsseldorf, Germany (2021)

17. Liu, B., et al.: An efficient method for antenna design optimisation based on evolutionary computation and machine learning techniques. IEEE Trans. Antenn. Propag. 62(1), 7–18 (2013)

18. Liu, B., et al.: Efficient global optimisation of microwave antennas based on a parallel surrogate model-assisted evolutionary algorithm. IET Microw., Antennas Propag. 13(2), 149–155 (2019)

19. Liu, B., Koziel, S., Ali, N.: SADEA-II: a generalised method for efficient global optimisation of antenna design. Journal of Computational Design and Engineering. 4(2), 86–97 (2017)

20. Akinsolu, M.O., et al.: A parallel surrogate model assisted evolutionary algorithm for electromagnetic design optimization. IEEE Transactions on Emerging Topics in Computational Intelligence. 3(2), 93–105 (2019)

21. Liu, B., et al.: An efficient method for complex antenna design based on a self-adaptive surrogate model-assisted optimisation technique. IEEE Trans. Antenn. Propag. 69(4), 2302–2315 (2021)

22. Grout, V., et al.: Software solutions for antenna design exploration: a comparison of packages, tools, techniques, and algorithms for various design challenges. IEEE Antenn. Propag. Mag. 61(3), 48–59 (2019)

23. Liu, B., Zhang, Q, Gielen, G.G.E.: A Gaussian process surrogate model assisted evolutionary algorithm for medium scale expensive optimisation problems. IEEE Trans. Evol. Comput. 18(2), 180–192 (2013)

24. Fusco, V., Yurduseven, O.: Ghost Image Removal Using Physical Layer Spatial Asymmetry in Frequency-Diverse Computational Imaging. 15th European Conference on Antennas and Propagation (EuCAP). IEEE (2021)

25. AbbasiBabar, M.A., et al.: Constant-ϵ_r lens beamformer for low-complexity millimetre-wave hybrid MIMO. IEEE Trans. Microw. Theor. Tech. 67(7), 2894–2903 (2019)

26. Katz, M.: Introduction to Geometrical Optics. World scientific (2002)

27. Stein, M.: Large sample properties of simulations using Latin hypercube sampling. Technometrics. 29(2), 143–151 (1987)

28. Dennis, J.E., Torczon, V.: Managing approximation models in optimisation. Multidisciplinary design optimization: State-of-the-art. 5, 330–347 (1997)